Diagnostic-Photographic Determination of Drag/Lift/Torque Coefficients of a High Speed Rigid Body in a Water Column

Peter C. Chu

Chenwu Fan

Naval Ocean Analysis and Prediction Laboratory,
Naval Postgraduate School,
Monterey, CA 94025

Paul R. Gefken
Polter Laboratory,
SRI International,
Menlo Park, CA 94025

Prediction of a rigid body falling through water column with a high speed (such as Mk-84 bomb) needs formulas for drag/lift and torque coefficients, which depend on various physical processes such as free surface penetration and bubbles. A semi-empirical method is developed in this study to determine the drag/lift and torque coefficients for a fast-moving rigid body in a water column. The theoretical part is to derive the relationships (called diagnostic relationships) between (drag, lift, and torque) coefficients and (position and orientation) of the rigid body from the three momentum equations and the three moment of momentum equations. The empirical part is to collect data of trajectory and orientation of a fast-moving rigid body using multiple high-speed video cameras (10,000 Hz). Substitution of the digital photographic data into the theoretical relationships leads to semi-empirical formulas of drag/lift and torque coefficients, which are functions of the Reynolds number, attack angle, and rotation rate. This method was verified by 1/12th Mk-84 bomb strike experiment with various tail configurations (tail section with four fins, two fins, and no fin and no-tail section) conducted at the SRI test site. The cost of this method is much lower than the traditional method using the wind tunnel. Various trajectory patterns are found for different tail configurations.
[DOI: 10.1115/1.3173767]

Keywords: body-flow interaction, drag coefficient, lift coefficient, torque coefficient, fast rigid body in water column, diagnostic-photographic method

1 Introduction

Prediction of a fast-moving rigid body in a water column has wide scientific significance and technical application. The dynamics of a rigid body allows one to set up six nonlinear equations for the most general motion: three momentum equations and three moment of momentum equations. The scientific studies of the hydrodynamic characteristics of a rigid body in a water column involve nonlinear dynamics, body and multiphase fluid interaction, free surface penetration, and stability theory.

The technical application of the hydrodynamics of a rigid body with high speed into fluid includes aeronautics, navigation, and civil engineering. Recently, the scientific problem about the movement of a rigid body in water column drew attention to the naval research. This is due to the threat of mine and maritime improvised explosive device (IED). Prediction of a fast falling rigid body in the water column contributes to the bomb breaching for mine and maritime IED clearance in surf and very shallow water zones with depth shallower than 12.2 m (i.e., 40 ft), according to U.S. Navy's standards.

To predict rigid body maneuvering in water column, accurate calculation of hydrodynamic forces and torques is difficult due to unknown drag, lift, and torque coefficients. Determination of these coefficients is crucial for the prediction [1–3]. Different from traditional methods used in aerodynamics, such as using the wind tunnel, we present a new efficient and low cost method to determine the drag, lift, and torque coefficients. This method consists of theoretical and empirical parts. The theoretical part is to establish dynamical relationships between hydrodynamic coefficients (e.g., drag, lift, and torque coefficients) and kinematics of the rigid body (e.g., position and orientation). The empirical part is to conduct experiments through shooting the rigid body into the water tank with high-speed video (HSV) cameras at 10,000 frames per second (fps) to record its underwater position and orientation. Semi-empirical formulas can be established for the drag, lift, and torque coefficients by substituting the digital data of rigid body's location and orientation from the HSV cameras into the dynamical relationships.

The rest of the paper is outlined as follows. Sections 2 and 3 describe the hydrodynamic forces, torques, and basic dynamics. Section 4 presents the diagnostic relationships for the drag/lift and torque coefficients, which were derived from the momentum and moment of momentum equations. Section 5 depicts the empirical method. Sections 6 and 7 show the semi-empirical formulas for the drag/lift and torque coefficients and the verification. Section 8 describes the tail section damage effects. Section 9 presents the conclusions.

2 Hydrodynamic Forces and Torques

2.1 Drag/Lift Forces. The earth-fixed coordinate system is used with the unit vectors $(\mathbf{i}, \mathbf{j})$ in the horizontal plane and the unit vector $\mathbf{k}$ in the vertical direction. Consider an axially symmetric rigid body such as a bomb falling through a water column. The two end-points of the body (i.e., head and tail points) are represented by $\mathbf{r}_h(t)$ and $\mathbf{r}_t(t)$. The difference between the two vectors in the nondimensional form

$$\mathbf{e} = \frac{\mathbf{r}_h - \mathbf{r}_t}{|\mathbf{r}_h - \mathbf{r}_t|} \tag{1}$$

is the unit vector representing the body's main axis direction (Fig. 1). The centers of mass (o_m) and volume (o_v) are located on the

Contributed by the Applied Mechanics Division of ASME for publication in the JOURNAL OF APPLIED MECHANICS. Manuscript received August 25, 2008; final manuscript received May 12, 2009; published online October 5, 2009. Review conducted by Nadine Aubry.

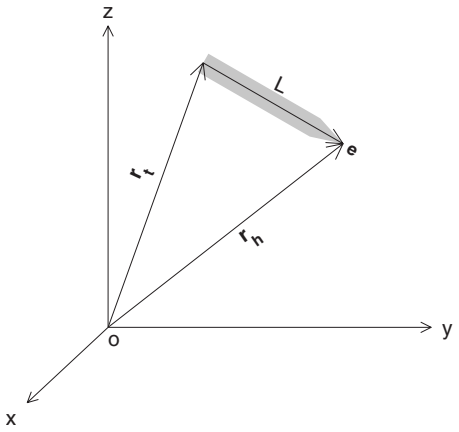

Fig. 1 Position vectors $\mathbf{r}_h$, $\mathbf{r}_t$, and the unit vector e

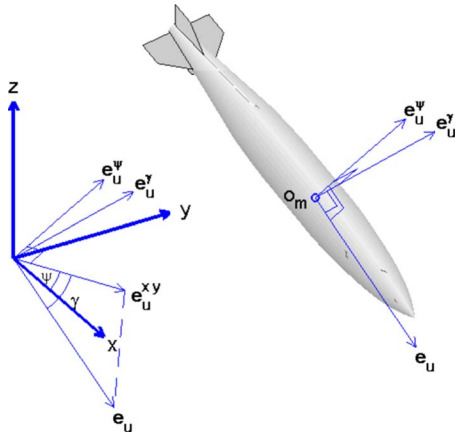

Fig. 3 Illustration of unit vectors ($\mathbf{e}_u$,$\mathbf{e}_u^{\psi}$,$\mathbf{e}_u^{\gamma}$, and $\mathbf{e}_u^{xy}$) with $\mathbf{e}_v^{xy}$ the projection of $\mathbf{e}_u$ on the *xy* plane

main axis with σ the distance between o_v and o_m, which has a positive (negative) value when the direction from o_v to o_m is the same (opposite) as the unit vector **e** (Fig. 2). The location (or called translation) of the body is represented by the position of o_m

$$\mathbf{r}(t) = x\mathbf{i} + y\mathbf{j} + z\mathbf{k} \tag{2}$$

The translation velocity is given by

$$\frac{d\mathbf{r}_o}{dt} = \mathbf{u}, \quad \mathbf{u} = U\mathbf{e}_u \tag{3}$$

where U and $\mathbf{e}_u$ are the speed and unit vector of the rigid-body velocity. Let β be the angle of the body's main axis with the horizontal plane, γ be the angle of the body's velocity **u** with the horizontal plane, and α be the attack angle between the direction of the main body axis (**e**) and the direction of the body velocity ($\mathbf{e}_u$) [4] (Fig. 2)

$$\alpha = \cos^{-1}(\mathbf{e}_u \bullet \mathbf{e}), \quad \beta = \sin^{-1}(\mathbf{e} \bullet \mathbf{k}), \quad \gamma = \sin^{-1}(\mathbf{e}_u \bullet \mathbf{k}) \tag{4}$$

Usually, the unit vector $\mathbf{e}_u$ is represented by (Fig. 3)

$$\mathbf{e}_u = \cos\ \gamma \cos\ \psi\mathbf{i} + \cos\ \gamma \sin\ \psi\mathbf{j} + \sin\ \gamma\mathbf{k} \tag{5}$$

where ψ is the azimuth angle. Differentiation of Eq. (5) with respect to t gives

$$\frac{d\mathbf{e}_u}{dt} = \frac{d\gamma}{dt}\mathbf{e}_u^{\gamma} + \frac{d\psi}{dt}\cos\ \gamma\mathbf{e}_u^{\psi} \tag{6}$$

where

$$\mathbf{e}_u^{\psi} = -\sin\ \psi\mathbf{i} + \cos\ \psi\mathbf{j}, \quad \mathbf{e}_u^{\gamma} = -\sin\ \gamma\cos\ \psi\mathbf{i} - \sin\ \gamma\sin\ \psi\mathbf{j} + \cos\ \gamma\mathbf{k} \tag{7}$$

are unit vectors. It is clear that

$$\mathbf{e}_u^{\psi} \perp \mathbf{e}_u, \quad \mathbf{e}_u^{\gamma} \perp \mathbf{e}_u, \quad \mathbf{e}_u^{\gamma} \perp \mathbf{e}_u^{\psi} \tag{8}$$

Let $\mathbf{V}_w$ be the water velocity. Water-to-body relative velocity **V** (called the relative velocity) is represented by

$$\mathbf{V} \equiv \mathbf{V}_w - \mathbf{u} \approx -\mathbf{u} = -U\mathbf{e}_u \tag{9}$$

Here, the water velocity is assumed much smaller than the rigid-body velocity. A third basic unit vector ($\mathbf{e}_m^h$) can be defined perpendicular to both **e** and $\mathbf{e}_u$

$$\mathbf{e}_m^h = \frac{\mathbf{e}_u \times \mathbf{e}}{|\mathbf{e}_u \times \mathbf{e}|} \tag{10}$$

The drag force ($\mathbf{F}_d$) is in the opposite direction of the rigid-body velocity. The lift force ($\mathbf{F}_l$) is in the plane constructed by the two vectors (**e** and $\mathbf{e}_u$) (i.e., perpendicular to $\mathbf{e}_m^h$) and perpendicular to $\mathbf{e}_u$, and therefore the lift force is in the same direction as $\mathbf{e}_m^h \times \mathbf{e}_u$. Both drag and lift forces, exerting on the center of volume, are represented by

$$\mathbf{F}_d = -f_d\mathbf{e}_u, \quad \mathbf{F}_l = f_l\mathbf{e}_l, \quad \mathbf{e}_l = \mathbf{e}_m^h \times \mathbf{e}_u \tag{11}$$

where f_d and f_1 are the magnitudes of the forces. The magnitudes (f_d,f_l) are represented by the drag law [5]

$$f_d = \tfrac{1}{2}C_d\rho A_w U^2, \quad f_l = \tfrac{1}{2}C_l\rho A_w U^2 \tag{12}$$

where ρ is water density; A_w is the under water projection area; C_d and C_l are the drag and lift coefficients, which are determined by the experiments.

Bomb is a fast-moving rigid body usually with four fins. Two fins in the same plane are called the pair of fins. For simplicity, these fins are treated approximately as the NACA0015 airfoils (Fig. 4) with known drag and lift coefficients [6]. Using these

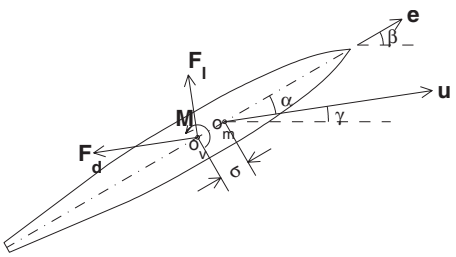

Fig. 2 Attack angle (α), angles (β,γ), center of volume (o_v), center of mass (o_m), and drag and lift forces (exerted on o_v). Note that σ is distance between o_v and o_m with positive (negative) value when the direction from o_v to o_m is the same (opposite) as the unit vector e.

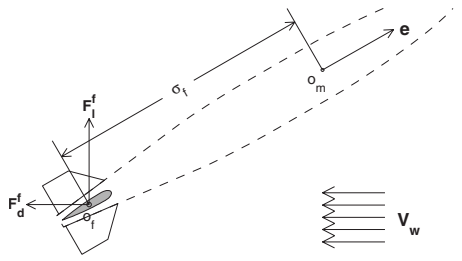

Fig. 4 Axial and cross-axial velocity ($\mathbf{u}_a^f$,$\mathbf{u}_c^f$), associated hydrodynamic forces on a pair of fins ($\mathbf{F}_a^f$,$\mathbf{F}_c^f$) and the distance between o_f and o_m (i.e., σ_f) with positive (negative) value when the direction from o_f to o_m is the same (opposite) as the unit vector e

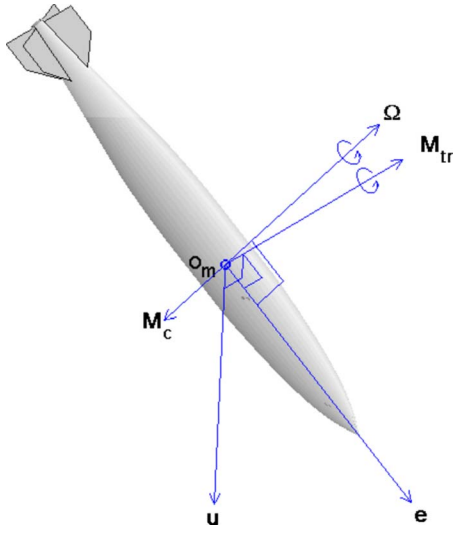

Fig. 5 Illustration of Ω, M_{tr}, and M_c

coefficients, the combined drag and lift forces on a pair of fins ($\mathbf{F}_c^f$) can be calculated. If the bomb has n pairs of fins, the total drag and lift forces on the fins are represented by $n\mathbf{F}_c^f$.

2.2 Hydrodynamic Torque. Since the drag/lift forces are exerted on the center of volume (o_v), the hydrodynamic torque (relative to center of mass, o_m) $\mathbf{M}_h$ is computed by

$$\mathbf{M}_h = -\sigma\mathbf{e} \times (\mathbf{F}_d + \mathbf{F}_l) - n\sigma_f\mathbf{e} \times \mathbf{F}_c^f + \mathbf{M}_{\text{tr}} + \mathbf{M}_{\text{rot}} \tag{13}$$

where the first two terms in the righthand side of Eq. (13) represent the torque by the drag and lift forces; $\mathbf{M}_{\text{tr}}$ is the antitranslation torque by the moment of drag/lift forces; and $\mathbf{M}_{\text{rot}}$ is the antirotation torque. $\mathbf{M}_{\text{tr}}$ is perpendicular to both $\mathbf{e}_u$ (the direction of $\mathbf{V}$) and $\mathbf{e}$ (the body orientation), and therefore it is in the same direction of the unit vector $\mathbf{e}_m^h$

$$\mathbf{M}_{\text{tr}} = M_{\text{tr}}\mathbf{e}_m^h \tag{14}$$

with M_{tr} being its magnitude calculated by the drag law [4]

$$M_{\text{tr}} = \tfrac{1}{2}C_m\rho A_w L_w U^2 \tag{15}$$

Here, C_m is the antitranslation torque coefficient.

2.3 Antirotation Torque. The antirotation torque acts as the rigid body rotates. Let $\mathbf{\Omega}^*$ be the rigid body's angular velocity vector, which is decomposed into two parts, with one along the unit vector $\mathbf{e}$ (bank angle) and the other $\mathbf{\Omega}$ (azimuthal and elevation angles) perpendicular to $\mathbf{e}$ (Fig. 5)

$$\Omega^* = \Omega_s\mathbf{e} + \mathbf{\Omega} \tag{16}$$

Let $\mathbf{e}_\omega$ be the unit vector in the direction of $\mathbf{\Omega}$

$$\Omega = \Omega\mathbf{e}_\omega, \quad \Omega = |\mathbf{\Omega}| \tag{17}$$

The unit vector $\mathbf{e}_\omega$ is perpendicular to $\mathbf{e}$

$$\mathbf{e}_\omega \cdot \mathbf{e} = 0 \tag{18}$$

Time rate of change of the unit vector $\mathbf{e}$ (main axis direction) is given by

$$\frac{d\mathbf{e}}{dt} = \mathbf{\Omega}^* \times \mathbf{e} = \mathbf{\Omega} \times \mathbf{e}. \tag{19}$$

Vector product between Eq. (19) and the unit vector $\mathbf{e}$ gives

$$\mathbf{e} \times \frac{d\mathbf{e}}{dt} = \mathbf{\Omega} = \Omega\mathbf{e}_\omega \tag{20}$$

Differentiation of Eq. (16) with respect to time t and use of Eq. (20) lead to [7]

$$\frac{d\mathbf{\Omega}^*}{dt} = \frac{d\Omega_s}{dt}\mathbf{e} + \Omega_s(\mathbf{\Omega} \times \mathbf{e}) + \frac{d\mathbf{\Omega}}{dt} \tag{21}$$

The antirotation torque ($\mathbf{M}_{\text{rot}}$) is against the rotation of the rigid body $\mathbf{\Omega}^*$. It can be decomposed into two parts

$$\mathbf{M}_{\text{rot}} = \mathbf{M}_s + \mathbf{M}_c \tag{22}$$

where the torque $\mathbf{M}_s$ (resistant to self-spinning, $\Omega_s\mathbf{e}$) parallels the main axis of the body (i.e., the unit vector $\mathbf{e}$)

$$\mathbf{M}_s = -M_s\mathbf{e}, \tag{23}$$

and the torque $\mathbf{M}_c$ is perpendicular to the unit vector $\mathbf{e}$

$$\mathbf{M}_c = -M_c\mathbf{e}_\omega, \quad \mathbf{e}_\omega \perp \mathbf{e}, \tag{24}$$

where M_s and M_c are the corresponding scalar parts. The drag law shows that [8]

$$M_s = \tfrac{1}{2}C_s\rho A_w L_w^3|\Omega_s|\Omega_s \tag{25}$$

$$M_c = \tfrac{1}{2}CF(\mu)\rho A_w L_w V_r^2, \quad \mu \equiv \Omega L_w/V \tag{26}$$

where the function $F(\mu)$ is obtained from the surface integration of torque due to cross-body hydrodynamic force (perpendicular to the body) [9]

$$F(\mu) \equiv \begin{cases} \dfrac{1}{6\mu} & \text{for } \mu \geq 1/2 \\ \left[\left(\dfrac{1}{4} - \mu^2\right) + \dfrac{4}{3}\mu^2 + \dfrac{1}{2\mu^2}\left(\dfrac{1}{16} - \mu^4\right)\right] & \text{for } \mu < 1/2 \end{cases} \tag{27}$$

Here, V_r is the projection of the water-to-body relative velocity on the vector $\mathbf{e}_r = \mathbf{e}_\omega \times \mathbf{e}$. Using Eq. (9) we have

$$V_r = \mathbf{V} \cdot \mathbf{e}_r = -U\mathbf{e}_u \cdot (\mathbf{e}_\omega \times \mathbf{e}) \tag{28}$$

In Eqs. (25) and (26), C_s is the torque coefficient for self-spinning; C is the drag coefficient due to cross-body flow. For a cylindrical body, the coefficient C is given by [10]

$$C = \begin{cases} 1.9276 + 8/\text{Re} & \text{if Re} \leq 12 \\ 1.261 + 16/\text{Re} & \text{if } 12 < \text{Re} \leq 180 \\ 0.855 + 89/\text{Re} & \text{if } 180 < \text{Re} \leq 2000 \\ 0.84 + 0.00003\,\text{Re} & \text{if } 2000 < \text{Re} \leq 12{,}000 \\ 1.2 - 4/\delta & \text{if } 12{,}000 < \text{Re} \leq 150000,\ \delta \geq 10 \\ 0.835 - 0.35/\delta & \text{if } 12{,}000 < \text{Re} \leq 150000,\ 2 \leq \delta < 10 \\ 0.7 - 0.08/\delta & \text{if } 12{,}000 < \text{Re} \leq 150{,}000,\ \delta < 2 \\ 1.875 - 0.0000045\,\text{Re} & \text{if } 150000 < \text{Re} \leq 350{,}000 \\ 1/(641550/\text{Re} + 1.5) & \text{if Re} > 350{,}000. \end{cases} \tag{29}$$

Here, δ is the aspect ratio of the rigid body; $\text{Re} = UD/\nu$, is the Reynolds number with D the effective diameter of rigid body.

3 Dynamics

3.1 Momentum Equation. Differentiation of Eq. (3) with respect to time t gives the acceleration of the rigid body

Table 1 Hopkinson scaling laws

Physical parameter	Symbol	Units	Required scaling for dimensionless quantities to have same value at all scales	Naturally scaled value with replica scaling in Earth's gravitational field
Length	L	L	L/S	L/S
Time	t	t	t/S	t/S
Mass	m	m	m/S^3	m/S^3
Displacement	x	L	x/S	x/S
Velocity	V	L/t	V	V
Acceleration	a	L/t^2	aS	aS
Density	ρ	m/L^3	ρ	ρ
Stress	σ	m/Lt^2	σ	σ
Strain	ε	1	ε	ε
Modulus	E	m/Lt^2	E	E
Strength	Y	m/Lt^2	Y	Y
Strain Rate	ε'	$1/t$	$\varepsilon' S$	$\varepsilon' S$
Gravity	g	L/t^2	gS	g
Viscosity	υ	$\sigma/\varepsilon' = m/Lt$	υ/S	υ
Fracture toughness	K	$\sigma L^{1/2} = m/L^{1/2}t^2$	$K/S^{1/2}$	K/S

$$\frac{d\mathbf{u}}{dt} = \frac{dU}{dt}\mathbf{e}_u + U\frac{d\mathbf{e}_u}{dt} \tag{30}$$

The momentum equation in the earth-fixed coordinate system is given by (Fig. 3)

$$m\left(\frac{dU}{dt}\mathbf{e}_u + U\frac{d\mathbf{e}_u}{dt}\right) = \mathbf{F} \tag{31}$$

where $\mathbf{F}$ is the resultant force consisting of

$$\mathbf{F} = \mathbf{F}_g + \mathbf{F}_b + \mathbf{F}_d + \mathbf{F}_l + n\mathbf{F}_c^f \tag{32}$$

Here,

$$\mathbf{F}_g = -mg\mathbf{k}, \quad \mathbf{F}_b = \rho\Pi g\mathbf{k} \tag{33}$$

are the gravity and buoyancy force and Π is the volume of the rigid body. For bomb without fin ($n=0$), the resultant force is represented by

$$\mathbf{F} = \mathbf{F}_g + \mathbf{F}_b + \mathbf{F}_d + \mathbf{F}_l \tag{34}$$

Inner products between Eq. (31) and the unit vectors ($\mathbf{e}_u, \mathbf{e}_u^{\psi}$, and $\mathbf{e}_u^{y}$ for $n=0$ lead to

$$m\frac{dU}{dt} = (\rho\Pi - m)g\mathbf{k} \bullet \mathbf{e}_u - f_d \tag{35}$$

$$mU\frac{d\gamma}{dt} = [(\rho\Pi - m)g\mathbf{k} + f_l\mathbf{e}_l] \bullet \mathbf{e}_u^{\gamma} \tag{36}$$

$$mU\cos\gamma\frac{d\psi}{dt} = [(\rho\Pi - m)g\mathbf{k} + f_l\mathbf{e}_l] \bullet \mathbf{e}_u^{\psi} \tag{37}$$

Here, we use Eq. (8) and the condition $\mathbf{e}_l \perp \mathbf{e}_v$ (i.e., the lift force perpendicular to the drag force). The vector $[(\rho\Pi - m)g\mathbf{k} + f_l\mathbf{e}_l]$ in Eqs. (36) and (37) can be represented by

$$[(\rho\Pi - m)\mathbf{k} + f_l\mathbf{e}_l] = \left(m\frac{dU}{dt} + f_d\right)\mathbf{e}_u + mU\frac{d\gamma}{dt}\mathbf{e}_u^{\gamma} + mU\cos\gamma\frac{d\psi}{dt}\mathbf{e}_u^{\psi} \tag{38}$$

with the magnitude of $(mdU/dt + f_d)$ in the direction of $\mathbf{e}_u$, $mUd\gamma/dt$ in the direction of $\mathbf{e}_u^{\gamma}$, and $mU\cos\gamma d\psi/dt$ in the direction of $\mathbf{e}_u^{\psi}$. Inner product of Eq. (38) by the unit vector $\mathbf{e}_l$ leads to

$$[(-m + \rho\Pi)g\mathbf{k} + f_l\mathbf{e}_l] \bullet \mathbf{e}_l = \left[mU\frac{d\gamma}{dt}\mathbf{e}_u^{\gamma} + mU\cos\gamma\frac{d\psi}{dt}\mathbf{e}_u^{\psi}\right] \bullet \mathbf{e}_l \tag{39}$$

where the condition ($\mathbf{e}_u \perp \mathbf{e}_l$) is used (see Eq. (11)).

3.2 Moment of Momentum Equation. The moment of momentum equation (relative to center of mass) is given by

$$\mathbf{J} \bullet \frac{d\boldsymbol{\Omega}^*}{dt} = \mathbf{M}_b + \mathbf{M}_h \tag{40}$$

where

$$\mathbf{M}_b = -\sigma\mathbf{e} \times (\rho\Pi g\mathbf{k}) \tag{41}$$

is the torque by buoyancy force (called the buoyancy torque). $\mathbf{J}$ is gyration tensor. In the body-fixed coordinate system $\mathbf{J}$ is a diagonal matrix [8]

$$\mathbf{J} = \begin{bmatrix} J_1 & 0 & 0 \\ 0 & J_2 & 0 \\ 0 & 0 & J_3 \end{bmatrix} \tag{42}$$

with J_1, J_2, and J_3 as the moments of inertia. For axially symmetric rigid body such as bomb, $J_2 = J_3$. Substitution of Eq. (13) into Eq. (40) and use of Eqs. (11) and (22) lead to

$$\mathbf{J} \bullet \frac{d\boldsymbol{\Omega}^*}{dt} = \mathbf{M}_s + \hat{\mathbf{M}} \tag{43}$$

where

$$\hat{\mathbf{M}} \equiv -\sigma\rho\Pi g\mathbf{e} \times \mathbf{k} - \sigma(f_d\mathbf{e} \times \mathbf{e}_u + f_l\mathbf{e} \times \mathbf{e}_l) - n\sigma_f f_c^f \mathbf{e} \times \mathbf{e}_c^f + \mathbf{M}_{\text{tr}} + \mathbf{M}_c \tag{44}$$

Since $\mathbf{M}_s$ is the antiself-spinning torque, which parallels the unit vector $\mathbf{e}$, and $\hat{\mathbf{M}}$ is the torque perpendicular to the unit vector $\mathbf{e}$, the moment of momentum Eq. (43) can be decomposed into two components with one parallel to $\mathbf{e}$ [11]

$$J_1\frac{d\Omega_s}{dt} = -M_s \tag{45}$$

and the other perpendicular to $\mathbf{e}$

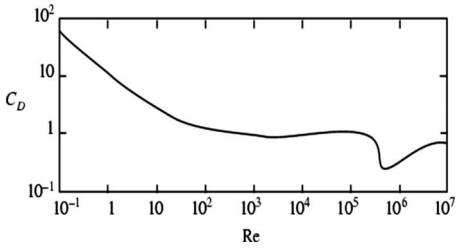

Fig. 6 Drag coefficient versus Reynolds number for a circular cross section (after Ref. [10])

$$\frac{d\boldsymbol{\Omega}}{dt} = \frac{\hat{\mathbf{M}}}{J_2} - \Omega_s(\boldsymbol{\Omega} \times \mathbf{e}) \tag{46}$$

where Eq. (24) is used. For a rigid body with very slow or no self-spinning (such as bomb), $\Omega_s \simeq 0$, Eq. (46) becomes

$$J_2 \frac{d\boldsymbol{\Omega}}{dt} = \hat{\mathbf{M}} \tag{47}$$

4 Determination of the Hydrodynamic Coefficients

The momentum Eqs. (35) and (39) can be rewritten by

$$C_d = \frac{2[(\rho\Pi - m)g\mathbf{k} \bullet \mathbf{e}_u - mdU/dt]}{\rho A_w U^2} \tag{48}$$

$$C_l = \frac{2[mU(\mathbf{e}_u^{\gamma} d\gamma/dt + \mathbf{e}_u^{\psi} \cos\ \gamma d\psi/dt) \bullet \mathbf{e}_l - (\rho\Pi - m)g\mathbf{k} \bullet \mathbf{e}_l]}{\rho A_w U^2} \tag{49}$$

Inner products of Eq. (47) by the unit vectors $\mathbf{e}_m^h$ (direction of $\mathbf{M}_{\text{tr}}$) for without fin ($n=0$) and $\mathbf{e}_\omega$ (direction of $\mathbf{M}_{\text{ae}}$) lead to

$$C_m = \frac{J_2 \dfrac{d\boldsymbol{\Omega}}{dt} \bullet \mathbf{e}_m^h + \sigma\rho\Pi g(\mathbf{e} \times \mathbf{k}) \bullet \mathbf{e}_m^h}{\dfrac{1}{2}\rho A_w L_w U^2} + CF(\Omega L_w / V_r)\frac{V_r^2}{U^2}\mathbf{e}_\omega \bullet \mathbf{e}_m^h$$

$$+ \frac{\sigma}{L_w}[C_d(\mathbf{e} \times \mathbf{e}_u) \bullet \mathbf{e}_m^h + C_l(\mathbf{e} \times \mathbf{e}_l) \bullet \mathbf{e}_m^h] \tag{50}$$

Equations (48)–(50) are used to determine the coefficients (C_d, C_l, and C_m). In the righthand sides of Eqs. (48)–(50), the unit vectors ($\mathbf{e}$, $\mathbf{e}_v$, and $\mathbf{e}_\omega$) are essential, and the other unit vectors ($\mathbf{e}_l$, $\mathbf{e}_m^h$, $\mathbf{e}_u^{\psi}$, and $\mathbf{e}_u^{\gamma}$) are derived.

Accurate prediction of a high-speed rigid body's location and orientation in the water column needs realistic values of the drag/lift and torque coefficients (C_d, C_l, and C_m). Among these coefficients, C_d, C_l, and C_m depend on the attack angle (α). Effects of special phenomena, such as surface impact, bubbles, and free surface penetration on the movement of rigid body, are represented in the change of these coefficients. Thus, if the time evolutions of unit vectors ($\mathbf{e}$, $\mathbf{e}_u$, and $\mathbf{e}_\omega$) and variables (x, y, z, U, ψ, and χ) are measured, time evolutions of the drag/lift and torque coefficients

Table 2 Drag coefficients between full-scale and 1/12-scale models

Flow type	Reynolds number	Drag coefficient	Full scale bomb velocity (m/s)	1/12 scale bomb velocity (m/s)
Laminar	$<10^3$	400–0.6	<0.002	<0.027
Laminar	10^3–3×10^5	0.6–0.5	0.002–0.67	0.027–7.8
Turbulent	$>3\times10^5$	<0.2	>0.67	>7.8

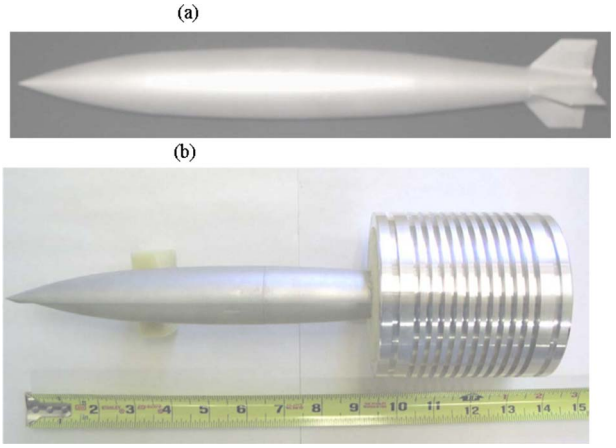

Fig. 7 Photography of 1/12th scale model Mk-84 bomb: (*a*) warhead with tail section and four fins and (*b*) sabot

(C_d, C_l, and C_m) can be obtained using the diagnostic relationships (48)–(50). The rotation rate Ω is calculated from the time series of (ψ, χ).

With large-amount of derived (C_d, C_l, and C_m) data, instantaneous relationships (semi-empirical formulas) can be established statistically between C_d, C_l, and C_m and basic parameters such as the attack angle α, Reynolds number (Re), and the rotation rate Ω. A traditional method for this purpose is to conduct experiments in the wind tunnel. Use of wind tunnel may be feasible for determining the drag/lift and torque coefficients of a rigid body in the air, but not realistic in the water especially the rigid body with high speed such as bomb.

5 Empirical Method

5.1 General Description. As alternative to the wind tunnel method, an empirical method is used to measure time evolutions of rigid body's head and tail points $\mathbf{r}_h(t)$ and $\mathbf{r}_t(t)$ using HSV cameras [12]. From the $\mathbf{r}_h(t)$, and $\mathbf{r}_t(t)$ data, the time series of the unit vectors ($\mathbf{e}$, $\mathbf{e}_u$, and $\mathbf{e}_\omega$), variables (x, y, z, U, ψ, χ), and attack angle (α) can be calculated using Eqs. (3)–(5) and (23). With the diagnostic relationships (48)–(50), time evolutions of the drag/lift and torque coefficients (C_d, C_l, and C_m) can be obtained.

5.2 Hopkinson Scaling Laws. The Hopkinson scaling laws are derived by normalizing the governing equations so that all terms are dimensionless, as shown in Table 1. The first three columns in the table below list the relevant physical parameters for dynamic structural and material response, their standard symbols, and their dimensional units. The first three (length, time, and mass) are basic parameters. The dimensions of all the other quantities can be expressed as powers of the basic parameters. The

Fig. 8 Overview experimental arrangement

Table 3 Summary of Mk-84 underwater trajectory experimental matrix

Launch No.	Model type	Water-entry velocity (m/s)	Water-entry impact angle (deg)
1	I (tail with four fins)	132	89.2
2	I (tail with four fins)	297	90.0
3	I (tail with four fins)	295	88.8
4	I (tail with four fins)	302	88.5
5	I (tail with four fins)	227	88.0
6	I (tail with four fins)	219	89.0
7	I (tail with four fins)	119	88.2
8	II (tail with two fins)	Impacted sabot	Stripper plate
9	II (tail with two fins)	Impacted sabot	Stripper plate
10	II (tail with two fins)	295	90.0
11	II (tail with two fins)	290	90.0
12	II (tail with two fins)	Impacted sabot	Stripper plate
13	IV (no tail)	297	85.7
14	IV (no tail)	301	90.0
15	IV (no tail)	301	88.7
16	III (tail with no fin)	304	90.0
17	III (tail with no fin)	297	87.0
18	III (tail with no fin)	291	88.1
19	II (tail with 2 fins)	297	90.0

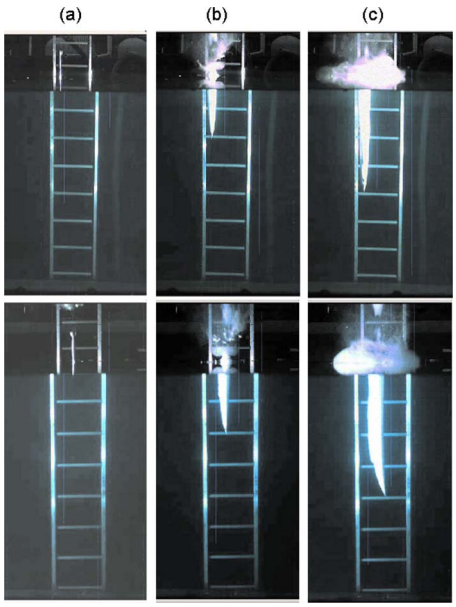

Fig. 9 Two HSV images for Launch-3 (Type-I) at water-entry velocity of 295 ms^{-1}: (*a*) initial water entry, (*b*) $t=22.8$ ms, and (*c*) $t=44.4$ ms

fourth column lists the required scaling for each of the parameters in dimensionless form to have the same value at all scales. That is, these entries define how each parameter should be scaled in order for the governing equations to give the same solution at all scales. For example, all of the length dimensions scale by the factor $1/S$. Just like length, time scales as $1/S$, but mass scales as $1/S^3$. The required scaling for the other quantities is then simply a matter of their actual dimensions in terms of L, t, and m. For example, velocity has dimensions L/t. Both L and t scale as $1/S$, so the ratio L/t is unchanged. Thus, velocities are the same at all scales. However, acceleration has dimensions L/t^2, and since both L and t scale as $1/S$, L/t^2 scales as S. Thus, accelerations at small scale are larger than at full scale by the inverse of the scale factor. A tremendous advantage of Hopkinson scaling is that density, stress, and strain are independent of scale.

The last column in the table lists the naturally scaled values of the parameters if the same materials are used and if the experiment is performed in a $1-g$ gravitational field. These can be compared with the previous column, which lists the scaling we desire for each parameter. Thus, all the parameters for which the last two columns are identical conveniently and naturally scale properly. However, the last three parameters—g, υ, and K—do not naturally scale properly. For example, if gravitational effects are important, gravity should be increased by the factor S. For the scale model Mk84 experiments described in this report, gravity mainly plays a role during the water surface waves that are generated during the initial impact. For the most part, these effects are second order and can be neglected. The effect of nonscaling viscosity or kinematic viscosity is related to the Reynolds number and drag coefficient value. The kinematic viscosity is typically a second-order effect at high velocities and may be a first-order effect at lower velocities, depending on the shape of the curve of drag coefficient versus Reynolds number. Lastly, the nonscaling of fracture toughness will not play a role, since there are no bombs casing failure mechanisms. When conducting experiments at a reduced scale, it is critical that all physical parameters of the problem are well understood. In water the Mk84 bomb will generate and travel in a cavitated column. The dynamics of motion are dominated by the pressure drag on the body produced by turbulent low-drag conditions, which will persist down to velocities of about 7.8 m/s for the scale models. For velocities less than 7.8 m/s, the dynamics of motion are dominated by laminar flow with frictional drag on the skin of the bomb casing in the form of viscous forces. The curve in Fig. 6 shows an empirical relationship between the drag coefficient and Reynolds number (ratio of inertial-to-viscous forces) for a given set of flow parameters around a circular cross section. This curve implies that the dominant forces acting on the submerged bomb may be determined as a function of the Reynolds number and, thus, of its velocity, throughout the trajectory. For exact similarity between the 1/12- and full-scale models, their respective Reynolds numbers must be equal. However, to achieve this exact similitude would require performing the scale-model experiments in a medium for which the kinematic viscosity has been reduced by the scale factor. The curve in Fig. 6 shows three distinct domains: for Reynolds numbers up to 10^3, the drag coefficient decreases monotonically to around 0.6, and for Reynolds numbers between 10^3 and 3×10^5 the drag coefficient is nearly constant at 0.5 to 0.6. Turbulent flow separation occurs for Reynolds numbers greater than 4×10^3, and the drag coefficient tends to be below 0.2.

Table 2 shows a comparison of the velocities at full scale and 1/12 scale for each of the three different domains. The first domain, in which the drag coefficient changes significantly with a change in Reynolds number, represents the primary region in which the scale models will not simulate the full-scale drag coefficient. However, this domain on the curve represents velocities of less than 0.002 m/s and is, therefore, insignificant for the practical purpose of our study. Instead, the majority of the bomb motion occurs in a turbulent flow region. The drag coefficient tends to be very small in this region, and it is likely that the small-scale models provide a good simulation of the full-scale models for velocities down to 7.8 m/s for 1/12 scale. The scale models overpredict the drag coefficient by a factor of about two or three for velocities between 7.8 m/s and 0.027 m/s for 1/12 scale. For these velocities, flow past the scale models is laminar with a constant drag coefficient of 0.5 to 0.6, whereas the full-scale model is experiencing turbulent flow with a drag coefficient of less than 0.2. In summary, Hopkinson scaling provides a good representation of the full-scale motion over about 95% of the velocity range between 450 m/s and 0 m/s.

5.3 Model Design and Construction. Details of the full-scale Mk84 with a guidance tail section were obtained from Boeing Corporation with the mass inertia properties for the complete

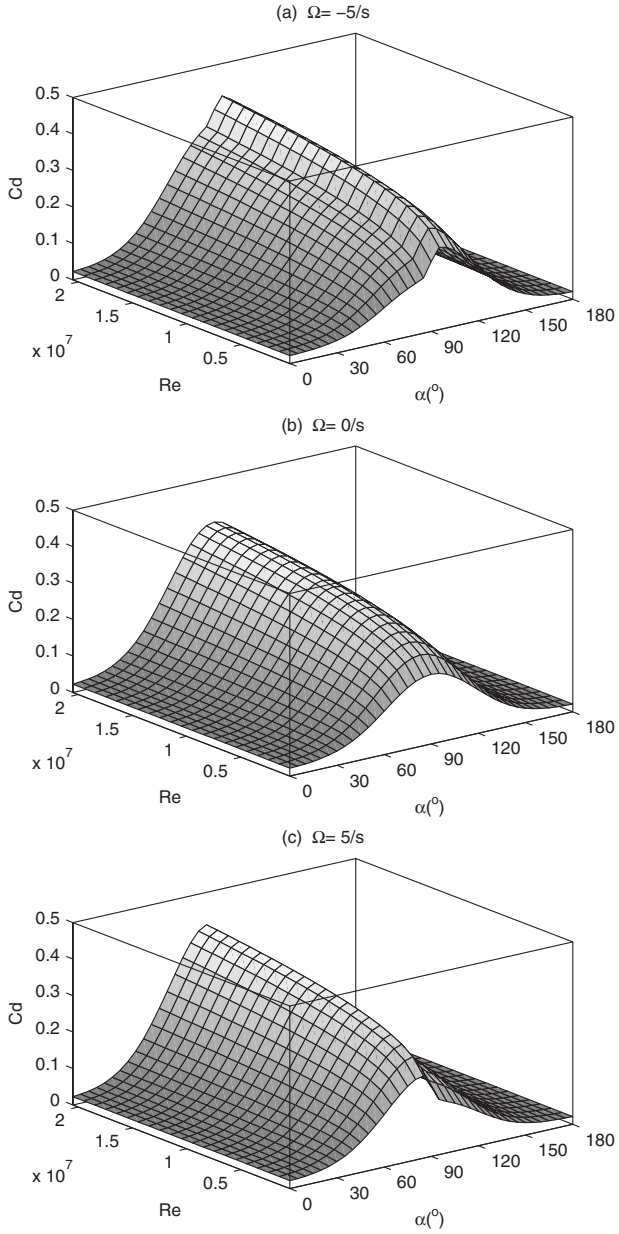

Fig. 10 Dependence of C_d on the Reynolds number (Re) and attack angle (α) for three different values of Ω: (*a*) −5 s^{-1}, (*b*) 0 s^{-1}, and (*c*) 5 s^{-1}

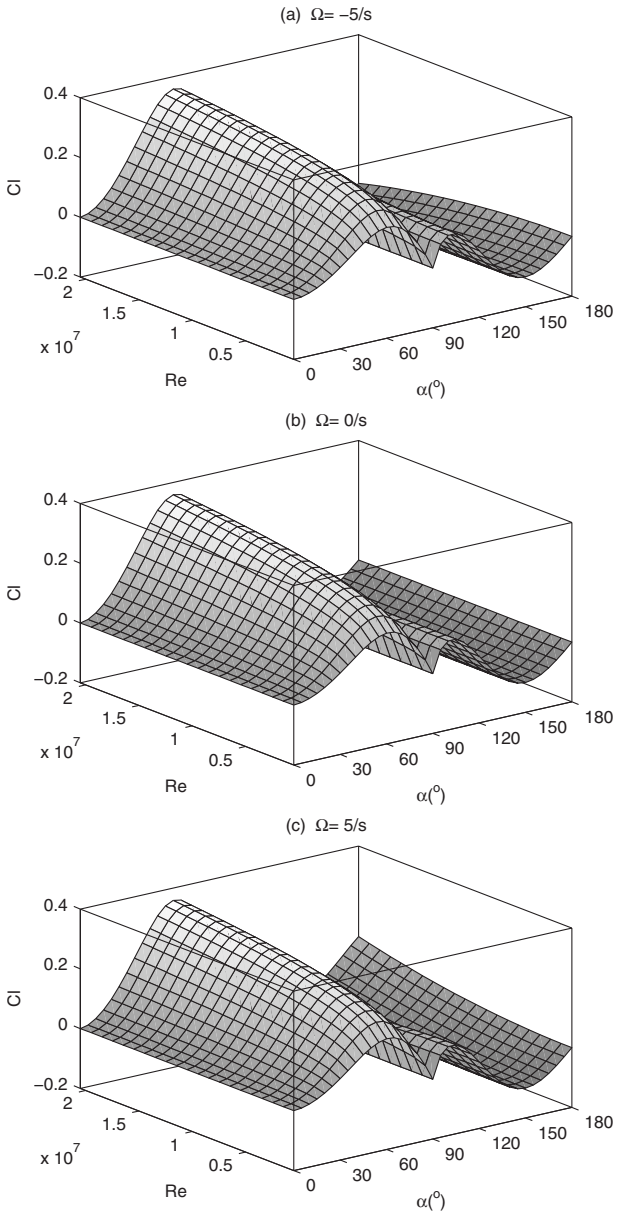

Fig. 11 Dependence of C_l on the Reynolds number (Re) and attack angle (α) for three different values of Ω: (*a*) −5 s^{-1}, (*b*) 0 s^{-1}, and (*c*) 5 s^{-1}

Mk84 warhead and tail section, as well as for the modifications to the tail section, including removal of two fins, four fins, and the complete tail section. We developed a closed form analytical model to determine the outer casing material and thickness and type of internal components and their location for the 1/12-scale model to match the scaled total mass, center of gravity and radius of gyration values for the Mk84 bomb with the different tail configurations. Here, the overall outer shape of the scaled Mk84 bomb represented an exact dimensional replica of the full-scale system. Figure 7 shows the overall design details of each model configuration. The outer casing was made from 7075-T6 aluminum. For the models with a tail section, the casing was fabricated in two pieces that were screwed together near the center point. To obtain the correct mass properties, a copper plug was inserted inside the model and then the remaining internal cavity was filled with a low density Epoxy. For all of the models with a tail section, only small differences in the copper plug size was required to match the mass properties. For these models the Epoxy had a density of 0.546 kg/m^3. For the model with no-tail section, two copper plugs were required and the Epoxy density had to be increased to 1.168 kg/m^3 by adding Tungsten powder. Four types of model Mk-84 bombs were constructed: Type-I (tail with 4 fins), Type-II (tail with two fins), Type-III (tail with no fins), and Type-IV (no tail).

5.4 Experiment Procedure. Two experiments were conducted to demonstrate the feasibility of this method with 1/12th scale model of the general purpose bomb (Mk-84) as the fast-moving rigid body. The first experiment was conducted at the Monterey Bay Aquarium Research Institute (MBARI) unmanned underwater vehicle test tank ($9.14 \times 13.72 \times 9.14$ m^3) filled with standard sea water [13,14]. The second experiment was conducted at a 6 m deep by 9 m diameter pool, located at the SRI's Corral Hollow Experiment Site [15]. A pneumatic launcher (gas gun) was used to shoot the 1/12th model Mk-84 bomb into the water tank in the first (second) experiment with velocities up to 100 m/s (454

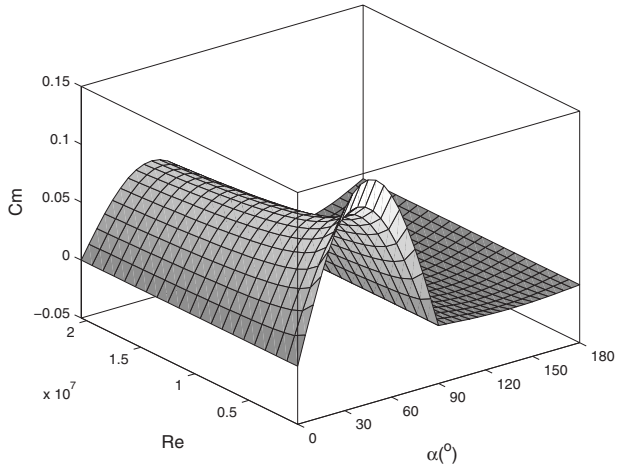

Fig. 12 Dependence of C_m on the Reynolds number (Re) and attack angle (α)

m/s) (Fig. 8). Since the implementation is very similar between the two experiments and the second experiment has much larger speed, the second experiment is presented here to illustrate this method.

Models of Mk-84 bombs with and without tail section are taken as examples to illustrate the methodology for determination of the drag/lift and torque coefficients (C_d, C_l, and C_m), and, in turn, the prediction of location and orientation of a fast-moving rigid body through the water column. The primary objective is to determine the Mk-84 trajectory through the very shallow water zone to provide an estimate of the maximum bomb-to-target standoff and required fuse delay time for optimum target lethality. Because it is possible that a portion, or all, of the guidance tail section may become separated from the warhead during water entry, it is necessary to determine the Mk-84 trajectory for a variety of different tail configurations, ranging from a warhead with a completely intact tail section and four fins to a warhead with the tail section completely.

Using the Hopkinson scaling laws, 1/12-scale Mk-84 bomb models were designed and constructed in SRI that matched the overall casing shape and mass inertial properties of the full-scale Mk-84 prototype. To model the different possible damaged tail configurations, we fabricated models that consisted of the warhead section with a complete tail section and four fins, a complete tail section and two fins, a complete tail section and no fins, and with the tail section removed. For the complete Mk-84 bomb system, including the warhead with tail section and four fins (Type-I), tail section and two fins (Type-II), tail section and no fin (Type-III), and no-tail section (Type-IV), were launched at different nominal water-entry velocity regimes from 120.0 m/s to 308.8 m/s. Table 3 summarizes the overall experimental matrix and water-entry conditions. Typically, the water-impact angle of entry was between 88 deg and 90 deg. In Launches 10, 11, and 12 the sabot failed to fully support the scale model within the gun during the launch phase, resulting in the scale model impacting the sabot stripper plate before impacting the water. Sequences of images from the two orthogonal HSV cameras were generated for each launch (Fig. 9).

The gas gun (0.10 m diameter and 1.52 m long) barrel was evacuated before launching the scale model to prevent an air blast from disturbing the water surface prior to the model impacting the water surface. At the end of the gas gun there was a steel ring to strip the sabot from the scale model. At high velocities there is some deviation from the theoretical calibration curve, which may be attributed to gas blow by around the sabot or friction. For the maximum gun operating pressure of 2,500 psi, we were able to

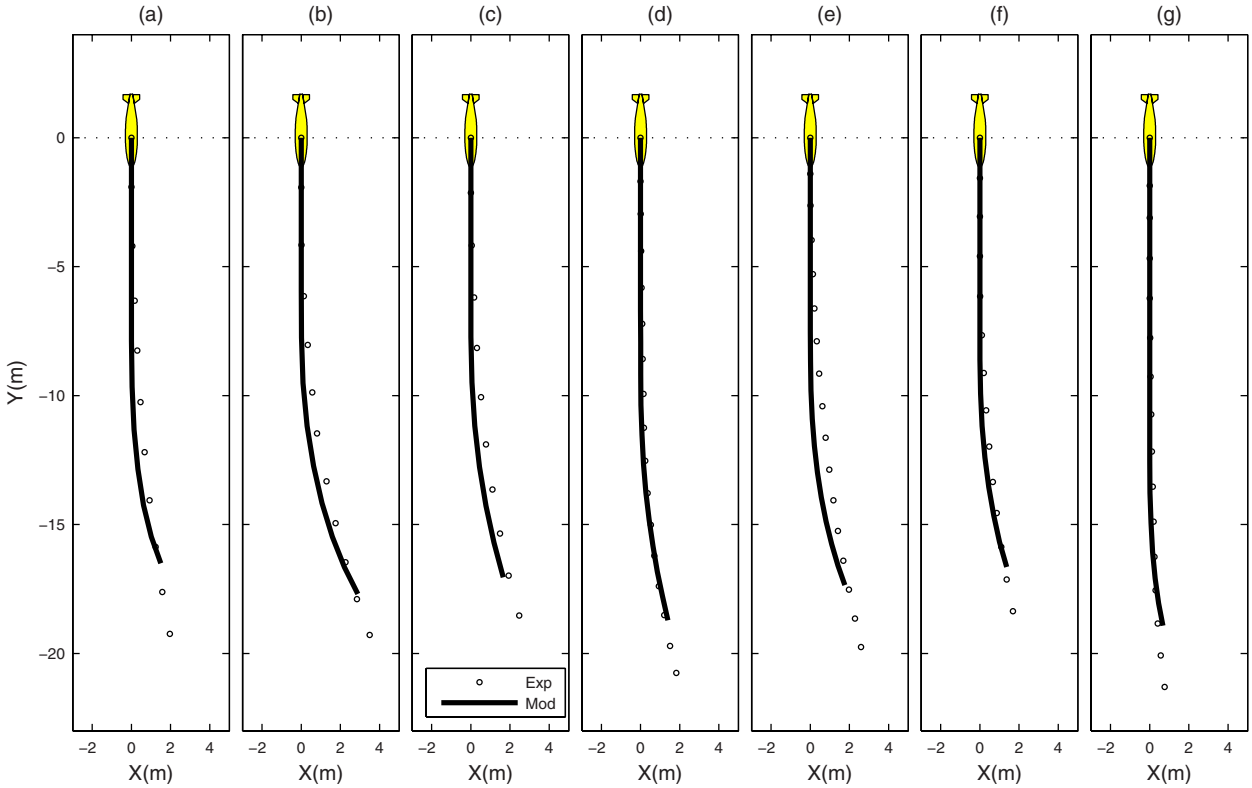

Fig. 13 Comparison between predicted and observed trajectories for Mk-84 warhead with tail section and four fins (Type-1) with initial water-entry speed: (*a*) 132 ms^{-1}, (*b*) 297 ms^{-1}, (*c*) 295 ms^{-1}, (*d*) 302 ms^{-1}, (*e*) 227 ms^{-1}, (*f*) 219 ms^{-1}, and (*g*) 119 ms^{-1}

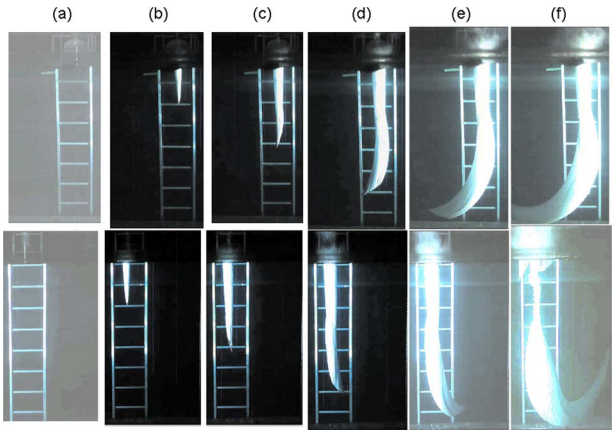

Fig. 14 Two HSV images for Launch-11 (Type-II) at water-entry velocity of 290 ms^{-1}: (a) initial water entry, (*b*) *t*=21.6 ms, (*c*) *t*=48.0 ms, (*d*) *t*=75.6 ms, (*e*) *t*=116.4 ms, and (*f*) *t* =344.4 ms

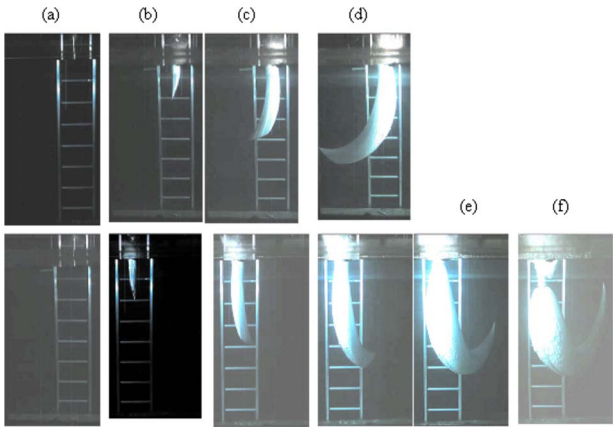

Fig. 16 Two HSV images for Launch-17 (Type-III) at water-entry velocity of 298 ms^{-1}: (*a*) initial water entry, (*b*) *t* =22.8 ms, (*c*) *t*=55.2 ms, (*d*) *t*=99.0 ms, (*e*) *t*=211.2 ms, and (*f*) *t*=376.2 ms. Note that for time longer than 99.0 ms, only one HSV camera got the pictures.

achieve a nominal water-entry velocity of about 305 m/s.

Two orthogonal periscope housings were positioned in the water tank to allow simultaneous above-water and below-water visualization of the model trajectory. The housings supported Phantom-7 HSV cameras, which were run at 10,000 fps. Five high-intensity short duration (30 ms) flash bulbs were used to front-light the scale model as it entered the water and traveled under water. The HSV cameras and flash bulbs were triggered at the time the sabot was released within the gun.

5.5 Data Retrieval. Upon completion of the launch phase, the video from each camera was converted to digital format. The digital video for each view was then analyzed frame by frame (10,000 Hz) in order to determine the bomb's position. The bomb's two-end (top and bottom) positions were input into a MATLAB generated grid, similar to the ones within the water tank. The first point to impact the water surface was always plotted first. This facilitated tracking of the initial entry point throughout the water column. Since only one ladder (Fig. 9) is used as the reference, 2D data in the $(y,\ z)$ plane were retrieved. This means that the x position of the projectile stays at zero.

After the data analysis, 16 time series of the unit vectors ($\mathbf{e}$, $\mathbf{e}_u$, and $\mathbf{e}_\omega$) variables $(x, y, z, U, \psi, \chi,$ and $\Omega)$, and attack angle (α) were obtained for the four types of the model Mk-84 bombs. All the experimental data have been converted to full-scale values using the Hopkinson scaling laws (see Table 1). For example, the length and time are multiplied by $S(=12)$, and the mass is multiplied by $S^3(=1728)$.

We divided the 16 time series into two groups: (a) Launches 13, 14, 15 (called the working data) for determining semi-empirical formulas for the drag/lift and torque coefficients (C_d, C_l, and C_m), and (b) rest of the data for evaluating the semi-empirical formulas (called evaluation data).

5.6 Source of Errors. There were several sources of error that hindered the determination of the bomb's exact position within the water column. Locations above or below the camera's focal point were subjected to parallax distortion. Placing the cameras as far back as possible, while still being able to resolve the individual grid squares, minimized this error. Second, the background grid (ladder in Fig. 9) was located behind the bomb's trajectory plane. This resulted in the bomb appearing larger than normal. This error was minimized by not allowing the plotted points to exceed the particular bomb's length. Third, an object injected into the water will generate an air cavity. This air cavity

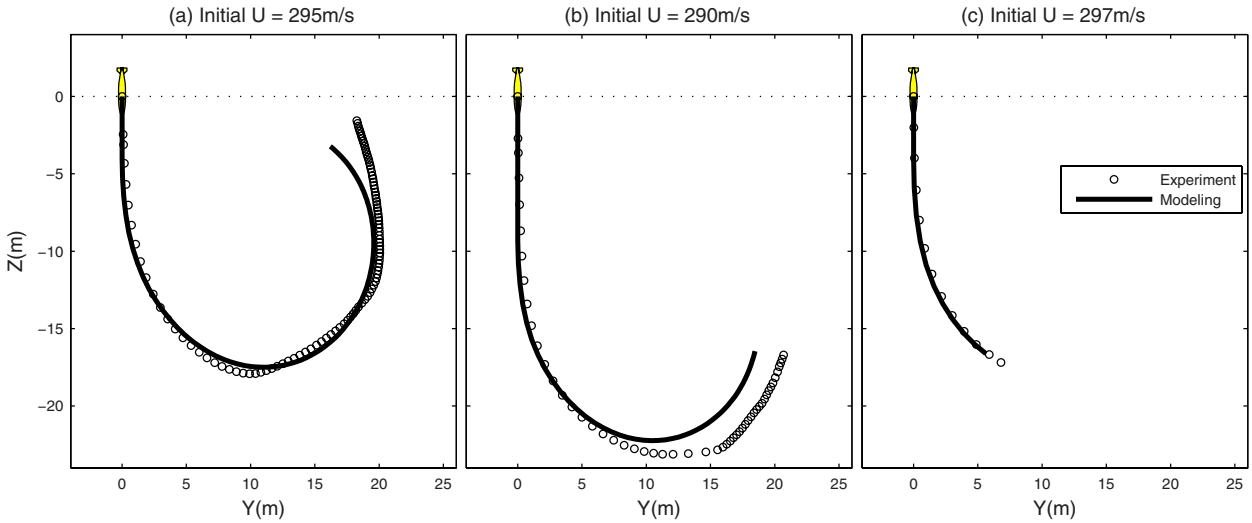

Fig. 15 Comparison between predicted and observed trajectories for Mk-84 warhead with tail section and two fins (Type-II) with initial water-entry speed: (*a*) 295 ms^{-1}, (*b*) 290 ms^{-1}, and (*c*) 297 ms^{-1}

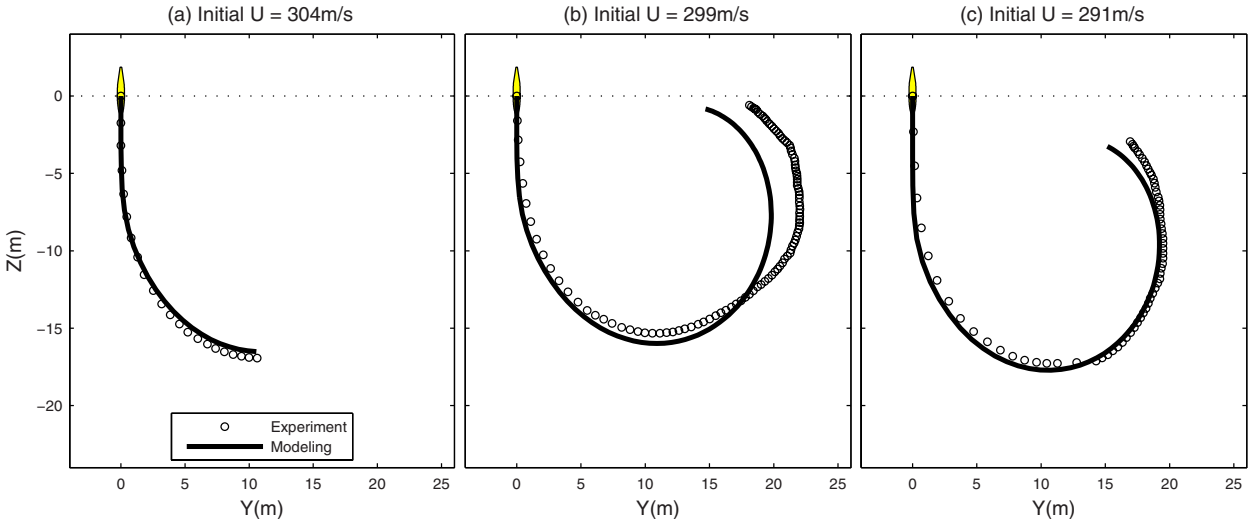

Fig. 17 Comparison between predicted and observed trajectories for Mk-84 warhead with tail section and no fin (Type-II) with initial water-entry speed: (*a*) 304 ms^{-1}, (*b*) 298 ms^{-1}, and (*c*) 291 ms^{-1}

can greatly affect the initial motion, particularly at very high speeds. The air cavity effect was deemed to be minimal when two 10,000 Hz HSV cameras were used.

6 Semi-Empirical Formulas

Statistical analysis was conducted on the working data set (Type-IV: Launch-13, -14, and -15) at each time step (data rate is 10,000 Hz) between (C_d, C_l, and C_m) and (Re, α, and Ω). The following semi-empirical formulas have been established

$$C_d = 0.02 + 0.35e^{-2(\alpha - \pi/2)^2}\left(\frac{\mathrm{Re}}{\mathrm{Re}^*}\right)^{0.2} + 0.008\Omega \sin\theta \quad (51)$$

$$C_l = \begin{cases} 0.35 \sin(\theta_1)\left(\dfrac{\mathrm{Re}}{\mathrm{Re}^*}\right)^{0.2} & \text{if } \alpha \le \dfrac{\pi}{2} \\ 0.1 \sin(\theta_2) - 0.015\Omega\left(\dfrac{\mathrm{Re}}{\mathrm{Re}^*}\right)^2 \sin(\theta_2^{0.85}) & \text{if } \alpha > \dfrac{\pi}{2} \end{cases} \quad (52)$$

$$C_m = \begin{cases} 0.07 \sin(2\alpha)\left(\dfrac{\mathrm{Re}^*}{\mathrm{Re}}\right)^{0.2} & \text{if } \alpha \le \dfrac{\pi}{2} \\ 0.02 \sin(2\alpha)\sqrt{\left(\dfrac{\mathrm{Re}}{\mathrm{Re}^*}\right)} & \text{if } \alpha > \dfrac{\pi}{2} \end{cases} \quad (53)$$

Here, $\mathrm{Re}^* = 1.810^7$, is the critical Reynolds number, and

$$\theta \equiv (\pi^{2.2} - (\pi - |\pi - 2\alpha|)^{2.2})^{1/2.2}\mathrm{sign}(\pi - 2\alpha) \quad (54)$$

$$\theta_1 = \pi\left(\frac{2\alpha}{\pi}\right)^{1.8}, \quad \theta_2 = 2\pi\left(\frac{2\alpha}{\pi} - 1\right)^{0.7} \quad (55)$$

The semi-empirical formulas (51)–(53) show that the drag/lift coefficients (C_d and C_l) depend more on Re and α and less on the rotation rate Ω. For the same attack angle (α), C_d increases with Re. For the same Re, C_d increases with α monotonically from 0 deg to 90 deg and reduces monotonically with α from 90 deg to 180 deg with a maximum value for α=90 deg (Fig. 10). The dependence of lift coefficient C_l on Re and α is a little complicated than C_d, especially for the attack angle larger than 90 deg (Fig. 11). The torque coefficient C_m depends only on Re and α (Fig. 12).

7 Verification of the Semi-Empirical Formulas

7.1 Experimental Results

7.1.1 Type-I. This type is for the complete Mk-84 bomb system, including the warhead with tail section and four fins. Seven launches (Launch-1–Launch-7) were conducted at different nominal water-entry velocity regimes (119–302 m/s). Figure 9 shows a sequence of images from the two orthogonal HSV cameras for a nominal velocity of 295 m/s (Launch-3). The cavitated column generated by the Mk-84 bomb motion consists of a tapered cone that has a maximum full-scale diameter at the end of the tail section of about 0.9 m. This is about a factor of two larger than the maximum bomb diameter of 0.45 m. This cavity shape was about the same for all of the initial water-entry velocities between 119 m/s and 302 m/s.

Figure 13 shows the comparison of bomb's translation and orientation for Type-I (Launch-1 to Launch-7) between the calculated and observed data. Both calculated and observed trajectories show similar patterns. For the low velocity regime of about 125

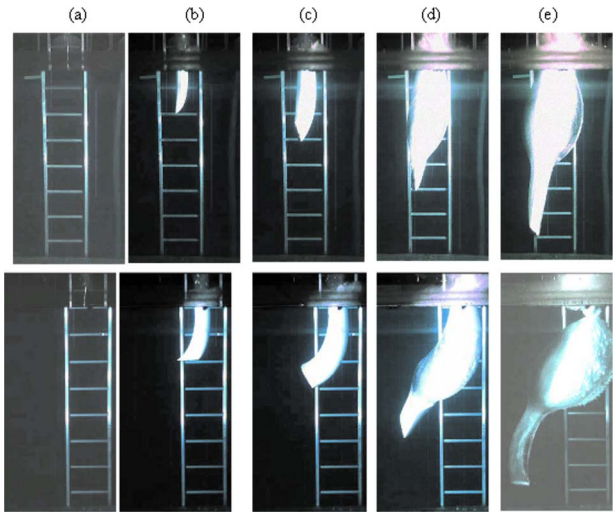

Fig. 18 Two HSV images for Launch-13 (Type-IV) at water-entry velocity of 296 ms^{-1}: (*a*) initial water entry, (*b*) *t* =30.0 ms, (*c*) *t*=51.6 ms, (*d*) *t*=155.4 ms, and (*e*) *t*=418.2 ms

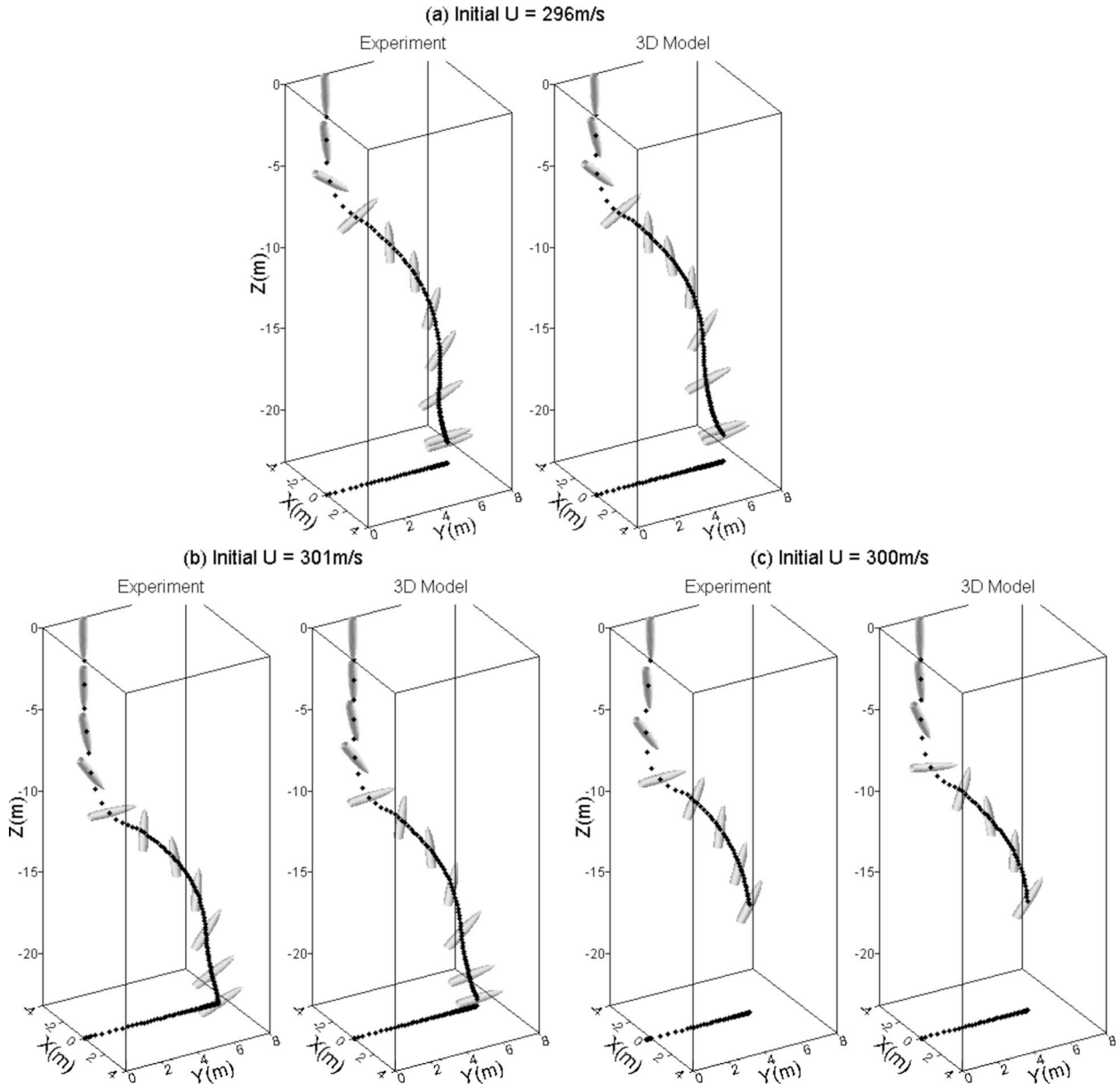

Fig. 19 Comparison between predicted and observed trajectories for Mk-84 warhead with no-tail section (Type-1V) with initial water-entry speed: (*a*) 296 ms^{-1}, (*b*) 301 ms^{-1}, and (*c*) 301 ms^{-1}

m/s (Launach-1 and Launch-7), at a full-scale depth of 12 m, the horizontal position ranged between 0.1 m (Launch-7, Fig. 13(*g*)) and 0.67 m (Launch-1, Fig. 13(*a*)). The bomb trajectories are quite stable without oscillation and tumbling no matter the water-entry velocity is high or low.

7.1.2 Type-II. This type is for the modified Mk84 bomb system including the warhead with a tail section and two fins. Three launches (Launch-10, -11, and -19) were conducted at an average water-entry velocity of about 294 m/s. Figure 14 shows a sequence of images (Launch-11) from the two orthogonal HSV cameras with a water-entry velocity of 290 m/s. The cavitated column generated by the bomb motion consists of a tapered cone that has a maximum full-scale diameter at the end of the tail section of about 0.9 m. This is about a factor of two larger than the maximum bomb diameter of 0.45 m. Thus, the initial cavity shape was about the same as for the model with a tail section and four fins, as described above.

Figure 15 shows the comparison of bomb's translation and orientation for Type-II (Launch-10, -11, and -19) between the calculated and observed data. Both calculated and observed trajectories show similar patterns. At full-scale depth of 12.2 m (i.e., 40 ft), the horizontal position ranged between 0.53 m (Launch-11) and 2.1 m (Launch-10). These values are about a factor of two larger than the values measured for Mk-84 bomb configuration with a tail section and four fins. Also, there seems to be no correlation between trajectory path and initial impact angle. The removal of two fins causes the bomb to eventually make a 180 deg turn and travel toward the surface. The 12.2 m depth is reached at about 45 ms after water entry.

7.1.3 Type-III. This type is for the modified Mk-84 bomb system, including the warhead with a tail section and no fin. Three launches (Launch-16, -17, and -18) were conducted at an average water-entry velocity of about 298 m/s. Figure 16 shows a sequence of images (Launch-17) from the two orthogonal HSV

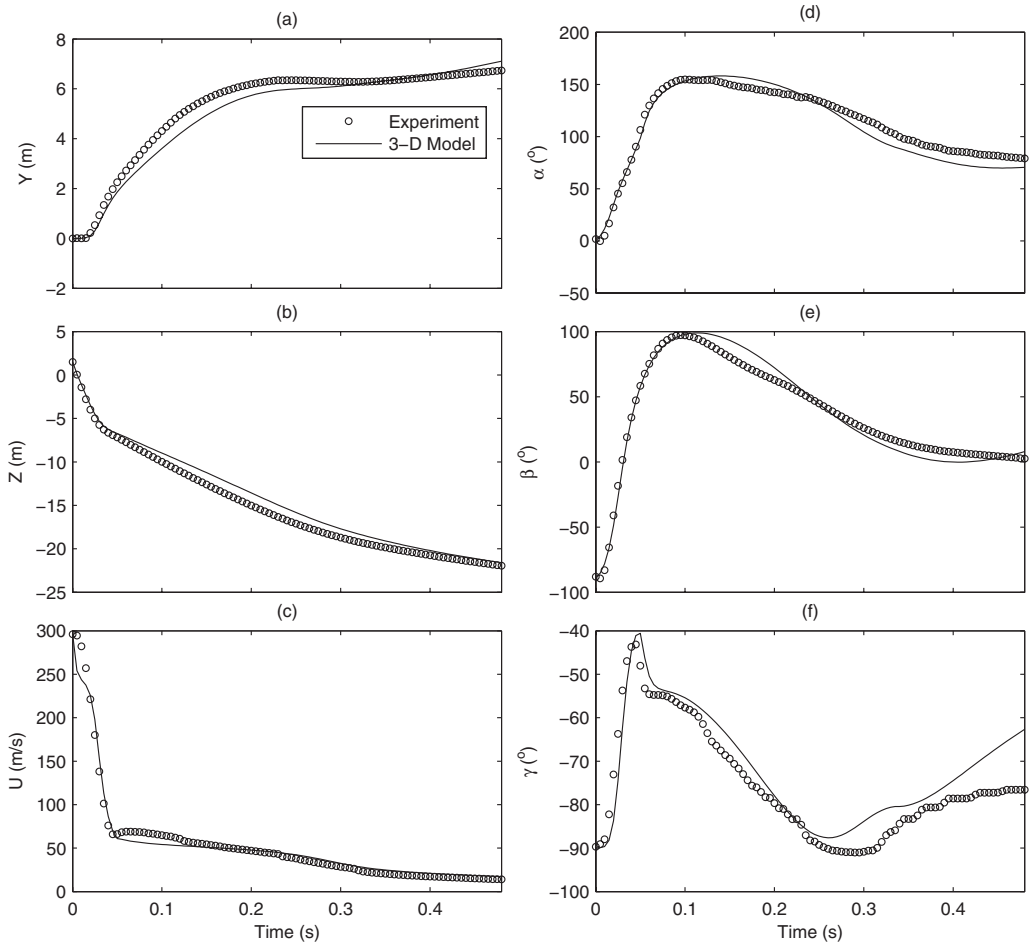

Fig. 20 Time-evolutions between predicted (solid) and observed (dotted) for Launch-13: (*a*) horizontal position (*y*) of o_m, (*b*) depth position (*z*) of o_m, (*c*) bomb speed (*U*), (*d*) angle γ, (*e*) angle β, and (*f*) attack angle α

cameras with a water-entry velocity of 297 m/s. The cavitated column generated by the bomb motion consists of a tapered cone that has a maximum full-scale diameter at the end of the tail section of about 0.9 m. This is about a factor of two larger than the maximum bomb diameter of 0.45 m. Thus, the initial cavity shape was about the same as for the model with a tail section and four fins and for the model with two fins, as described above.

Figure 17 shows the comparison of bomb's translation and orientation for Type-III (Launch-16, -17, and -18) between the calculated and observed data. Both calculated and observed trajectories show similar patterns. At full-scale depth of 12.2 m (i.e., 40 ft), the horizontal position ranges between 2.1 m (Launch-18) and 3.5 m (Launch-17). These values are about a factor of 9.5 and 3.5, respectively, larger than the values measured for an Mk-84 warhead with a tail section and four fins. Also, there seems to be no correlation between trajectory path and angle of impact. As shown in Figs. 15 and 16, the removal of four fins causes the bomb eventually to make a 180 deg turn and travel toward the surface in a manner similar to the trajectory for a bomb with a tail section and two fins. The 12.2 m depth is reached at about 47 ms after water entry. In general, the model with a tail section and no fins shows a decrease in overall trajectory stability compared with a model with a tail section and two fins. This is evident primarily through larger horizontal positions.

7.1.4 Type-IV. This type is for the modified Mk-84 bomb system, including the warhead and no-tail section. Three launches (Launch-13, -14, and -15) were conducted at an average water-entry velocity of about 299 m/s. Figure 18 shows a sequence of images (Launch-13) from the two orthogonal HSV cameras with a water-entry velocity of 297 m/s. The cavitated column generated by the bomb motion consists of a tapered cone that has a maximum full-scale diameter at the end of the tail section of about 0.9 m. This is about a factor of two larger than the maximum bomb diameter of 0.45 m. Thus, the initial cavity shape was about the same as for the model with a tail section (four, two, and no fins), as described above.

7.2 Model-Data Intercomparison. The momentum equations (35)–(37) and the moment of momentum equations (45) and (46) were integrated numerically integrated using Eqs. (51)–(53) for C_d, C_l, and C_m and the same parameters (such as the density ratio, length, radius, the center of volume, and the center of mass) and the drop initial conditions (speed and orientation) as in Type-III (tail without fin) and Type-IV (no tail) (see Table 3). The validity of the semi-empirical formulas (51)–(53) are verified through a comparison between calculated and observed bomb trajectories, orientations, and velocities.

Figure 19 shows the comparison of bomb's translation and orientation for Type-IV (Launch-13, -14, and -15) between the calculated and observed data. Both calculated and observed trajectories show similar patterns. At full-scale depth of 12.2 m (i.e., 40 ft), the bomb has rotated 180 deg such that the bomb is moving tail first. When the nose reaches a depth of 12.2 m, the nose horizontal position is between 5.5 m and 7.2 m. Launch-13 had a deviation of 4.3 deg from the vertical water-entry angle, which was the largest deviation in all of the launches. However, com-

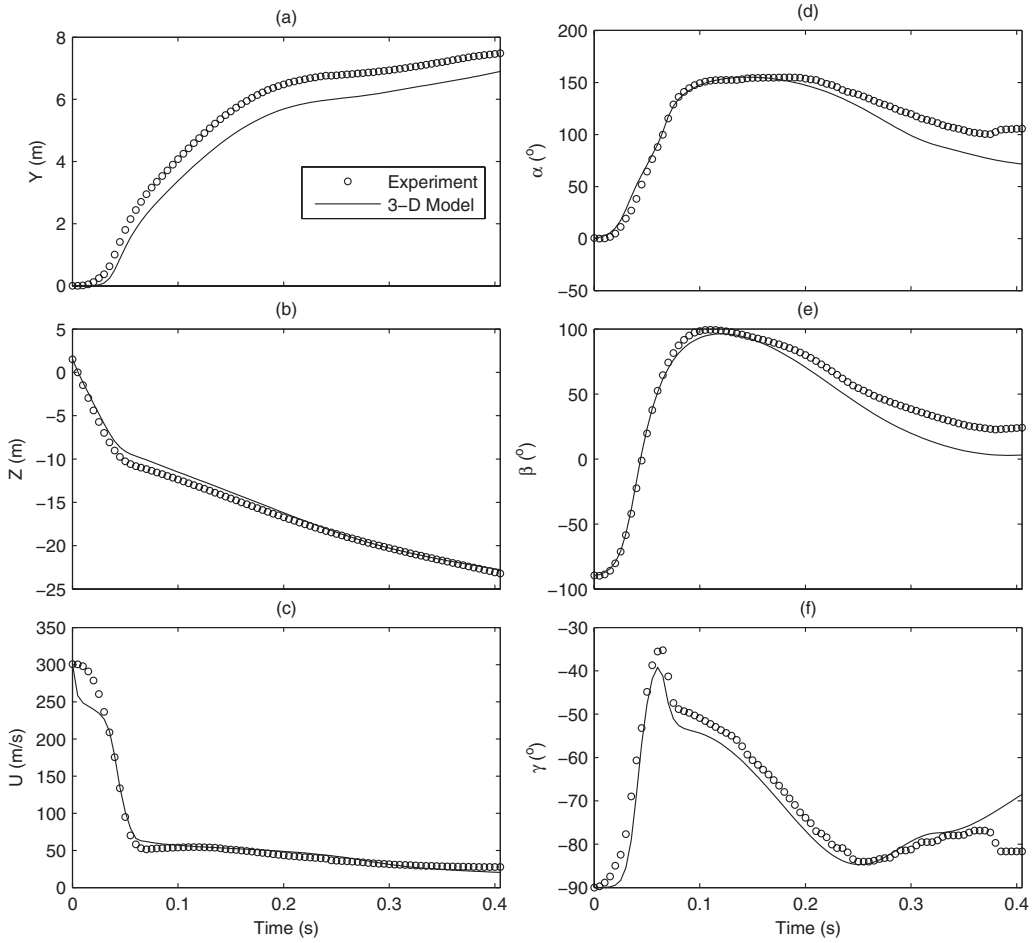

Fig. 21 Time-evolutions between predicted (solid) and observed (dotted) for Launch-14: (*a*) horizontal position (*y*) of o_m, (*b*) depth position (*z*) of o_m, (*c*) bomb speed (*U*), (*d*) angle γ, (*e*) angle β, and (*f*) attack angle α

parison of the trajectories in Launch-13 and Launch-14, in which a 90 deg water-entry angle was obtained, indicates that there is no correlation between impact angle and trajectory path. Thus, the trajectory motion is dominated by instability of the bomb within the cavitated region. Different from the Mk-84 bomb with a tail section and no fin (or two fins), the Type-IV bombs never move up toward the surface (Fig. 19). Although the model is fully 3D, in order to compare it with the 2D data set (see Sec. 5.5), only the 2D components in the (y, z) plan were computed. That is why the x position of the projectile stays zero in Fig. 19.

Figures 20–22 show the comparison between predicted and observed time evolutions of the horizontal shift (y) and depth position (z) of the center of mass (o_m), bomb speed (U), and angles (α, β, γ). At the water entry, the horizontal shift (y) is set to zero. The predicted values of these variables are consistent to the corresponding observed values. This confirms the validity of the semi-empirical formulas (53)–(55) for drag/lift and torque coefficients (C_d, C_l, and C_m). The three launches show the same interesting results. The bomb nose reaches the 12.2 m depth at about 110 ms after water entry. At this depth the bomb nose velocity decreased by about 82%. The horizontal deviation (y) of o_m increases rapidly at first and then slowly with time, and about 6 m from the entry point as the bomb reached the depth of 12.2 m.

8 Tail Section Damage Effects

The experiments conducted with different tail configurations were performed to determine the effects on bomb trajectory for different possible postulated damage levels to the tail section. Because the tail section is comprised mostly of internal stiffeners with an external skin, it may be weaker than the warhead section and, therefore, may be damaged during initial water entry or during tail slap within the cavitated region. Figure 23 shows the maximum measured trajectories for each tail configuration for a nominal water-entry velocity of about 297 ms^{-1}, i.e., Launch-2 (Type-I), Launch-19 (Type-II), Launch-17 (Type-III), and Launch-13 (Type-IV).

Table 4 summarizes data comparison of the overall trajectory behavior for the different tail configurations. For each trajectory parameter we show the value associated with a particular tail configuration and the percentage difference compared with a complete bomb having a tail section and four fins. The horizontal position shift y (noting that $y=0$ at the water entry) significantly increases with increased levels of damage to the tail section. For a model with a tail section and two fins, no fins, and no-tail section, the horizontal position values increase by 120%, 259%, and 575% (i.e., from 0.9 m to 2.12 m, 3.46 m, and 6.50 m), respectively. With regard to travel time at 12.2 m depth, only the no-tail configuration shows a significant increase of 179% (from 46.2 ms to 129. 5 ms).

9 Conclusions

A new dynamic-photographic method has been developed to determine the drag/lift and torque coefficients (C_d, C_l, and C_m) of a fast-moving rigid body in the water column. This method contains two parts: (1) establishment of the diagnostic relationship between C_d, C_l, and C_m and the rigid body's trajectory and orien-

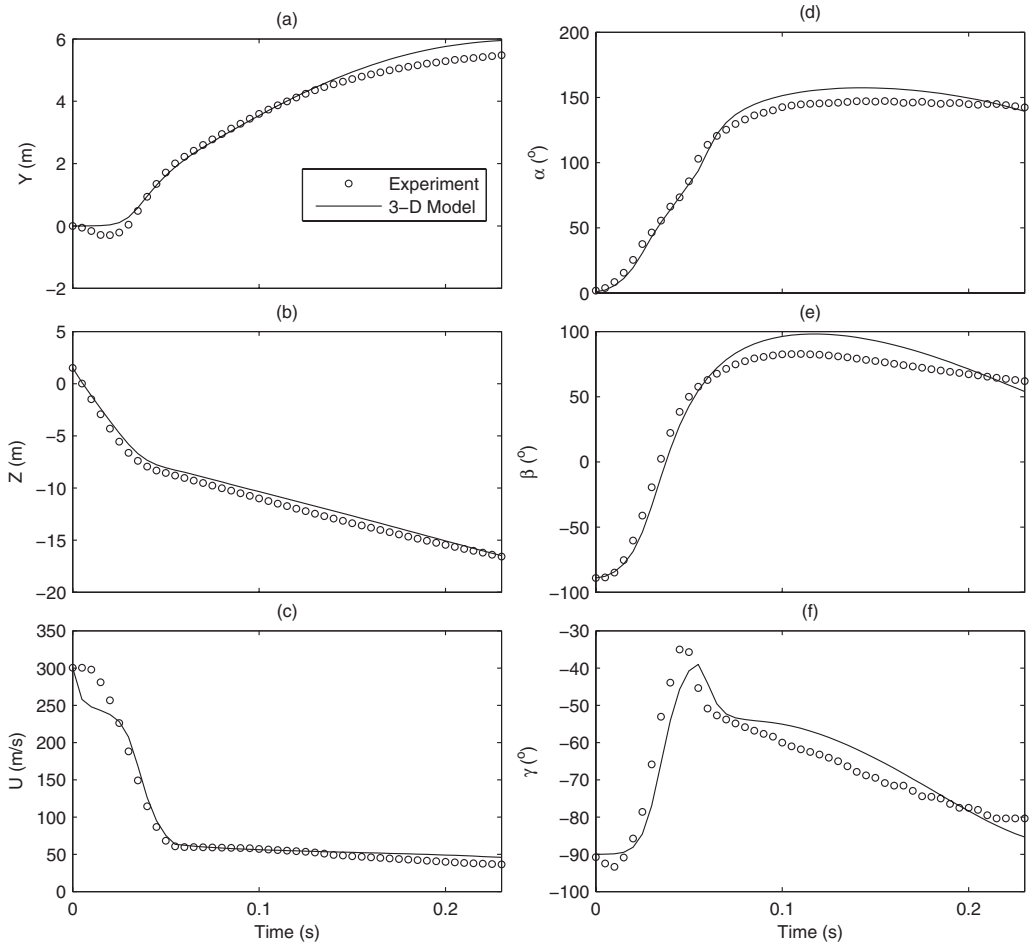

Fig. 22 Time-evolutions between predicted (solid) and observed (dotted) for Launch-15: (*a*) horizontal position (*y*) of o_m, (*b*) depth position (*z*) of o_m, (*c*) bomb speed (*U*), (*d*) angle γ, (*e*) angle β, and (*f*) attack angle α

tation, and (2) data collection of trajectory and orientation of a fast-moving rigid body using multiple high-speed video cameras (10,000 Hz). Using the digital photographic data, semi-empirical formulas of C_d, C_l, and C_m versus Reynolds number, attack angle, and rotation rate can be established. The cost of this method is much lower than the traditional method using the wind tunnel to determine C_d, C_l, and C_m.

To demonstrate the feasibility and powerfulness of this method, an experiment was conducted with 1/12th scale model of the general purpose bomb (Mk-84) as the fast-moving rigid body at a 6 m deep by 9 m diameter pool, located at the SRI's Corral Hollow Experiment Site. A gas gun was used to shoot the 1/12th model Mk-84 bomb into the water tank with velocities up to 304 ms^{-1}. Four types of Mk-84 model bombs were used for a total of 16 launches for the experiment: warhead with tail section and four fins (Type-1), with tail section and two fins (Type-1I), with tail section and no fin (Type-1II), and with no-tail section (Type-IV). Among them, data from three launches in Type-IV were used to get the semi-empirical formulas for C_d, C_l, and C_m. The rest of data were used for verification.

The momentum equations and moment of momentum equations were integrated with the same parameters (such as the density ratio, length, radius, the center of volume, and the center of mass) and the drop initial conditions (speed and orientation) as in the observations after using the semi-empirical formulas for C_d, C_l, and C_m. Consistency between calculated and observed bomb trajectories, orientations, and velocities show the powerfulness of this method.

Both calculated (solving dynamic equations with the semi-empirical formulas) and experimental data show similar results. The cavitated column generated by the Mk-84 bomb motion consists of a tapered cone that has a maximum full-scale diameter at the end of the tail section of about 0.9 m. This is about a factor of 2 larger than the maximum bomb diameter of 0.45 m. This cavity shape was about the same for all of the initial water-entry velocities and four types of model bombs.

The horizontal nose position significantly increases with increased levels of damage to the tail section. For a model with a tail section and two fins, no fins, and no-tail section, the horizontal position values increase by 120%, 259%, and 575%, respectively. With regard to travel time at 12.2 m (i.e., 40 ft) depth, only the no-tail configuration shows a significant increase of 179%.

For bomb with a tail section and four fins, its trajectories are quite stable without oscillation and tumbling whether the water-entry velocity is high or low. Removal of two fins causes the bomb to eventually make a 180 deg turn and to travel toward the surface. Although having a similar trajectory pattern (i.e., making a 180 deg turn and traveling toward the surface), the removal of four fins shows a decrease in overall trajectory stability compared with a model with a tail section and two fins. This is evident primarily through larger horizontal positions. For Mk-84 bomb without a tail section, the bomb has rotated for 180 deg at full-scale depth of 12.2 m, such that the bomb moves tail first. Different from the Mk-84 bomb with a tail section and no fin (or two fins), the Mk-84 bombs without a tail section never move up toward the surface.

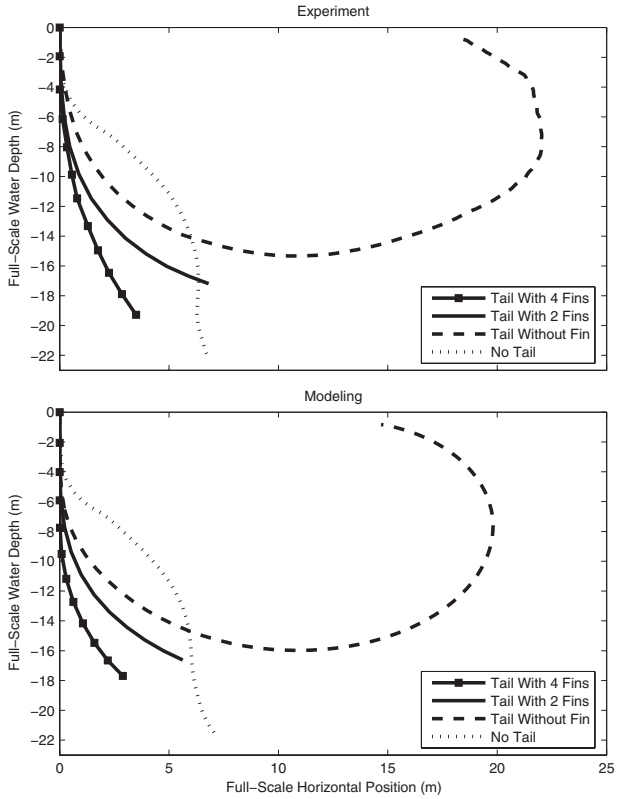

Fig. 23 Trajectories for Mk-84 warhead with different tail configurations

Acknowledgment

The Office of Naval Research Breaching Technology Program (Grant No. N0001405WR20209) and Naval Oceanographic Office supported this study. The program manager is Brian Almquist.

Table 4 Horizontal position shift and travel time at depth of 12.2 m (i.e., 40 ft) for Mk-84 warhead with different tail configurations

Model type	Horizontal position shift y (m)	Travel time (ms)
Tail with four fins	0.96	46.2
Tail with two fins	2.12	46.2
Tail with nonfins	3.46	49.8
No tail	6.50	129.5

References

[1] Chu, P. C., and Fan, C. W., 2006, "Prediction of Falling Cylinder Through Air-Water-Sediment Columns," ASME J. Appl. Mech., **73**, pp. 300–314.
[2] Chu, P. C., and Fan, C. W., 2005, "Pseudocylinder Parameterization for Mine Impact Burial Prediction," ASME J. Fluids Eng., **127**, pp. 1215–1220.
[3] Chu, P. C., (2009), "Mine Impact Burial Prediction From One to Three Dimensions," Appl. Mech. Rev., **62**(1), p. 010802.
[4] Munson, B. R., and Cronin, D. J., 1998, "Airfoils and Wings," *The Handbook of Fluid Dynamics*, R. W. Johnson, ed., CRC Press, New York.
[5] Von Mises, R., 1959, *Theory of Flight*, Dover, New York, pp. 564–585.
[6] Klimas, P. C., 1992, "Tailored Airfoils for Vertical Axis Wind Turbines," Sandia Report No. SAND84–1062.
[7] Chu, P. C., and Fan, C. W., 2007, "Mine Impact Burial Model (IMPACT35) Verification and Improvement Using Sediment Bearing Factor Method," IEEE J. Ocean. Eng., **32**(1), pp. 34–48.
[8] Chu, P. C., Fan, C. W., Evans, A. D., and Gilles, A., 2004, "Triple Coordinate Transforms for Prediction of Falling Cylinder Through the Water Column," ASME J. Appl. Mech., **71**, pp. 292–298.
[9] Rouse, H., 1938, *Fluid Mechanics for Hydraulic Engineers*, McGraw-Hill, New York.
[10] Crowe, C. T., Roberson, J. A., and Elger, D. F., 2001, *Engineering Fluid Mechanics*, Wiley, New York.
[11] White, F. M., 1974, *Viscous Fluid Flow*, McGraw-Hill, New York.
[12] Chu, P. C., Gilles, A., and Fan, C. W., 2005, "Experiment of Falling Cylinder Through the Water Column," Exp. Therm. Fluid Sci., **29**, pp. 555–568.
[13] Chu, P. C., Ray, G., Fleischer, P., and Gefken, P., 2006, "Development of Three Dimensional Bomb Maneuvering Model," Seventh Monterey International Symposium on Technology and Mine Problems, NPS, Monterey, CA, May 1–4, p. 10, DVD-ROM.
[14] Ray, G., 2006, "Bomb Strike Experiments for Mine Countermeasure," MS thesis, Naval Postgraduate School, Monterey, CA
[15] Gefken, P. R., 2006, "Evaluation of Precision-Guided Bomb Trajectory Through Water Using Scale-Model Experiments," SRI Final Technical Report No. PYU-16600.